# Multistatic lidar measurements of non-spherical aerosols

Hans D. Hallen, Brandon J. N. Long, D. Adam Hook, Garrett E. Pangle, and C. Russell Philbrick
Physics Department, NC State University, Raleigh NC 27695-8202

## ABSTRACT

Lidar is a powerful tool for measuring the vertical profiles of aerosols in the atmosphere using Rayleigh and Raman lidar techniques. Bistatic lidar can be used to obtain the angular structure of the scattered light. When the aerosols are uniformly distributed, this information can be analyzed to provide particle size distribution information. However, dusts tend to be irregularly shaped particles with varied composition. We investigate the impact of the irregular shape using optical scattering at several wavelengths, scanning electron microscopy, and T-matrix calculations. In particular, we study the rapid loss of Mie scattering resonances as the particle shape departs from spherical. Different size distributions produced by different size-cuts of Arizona Road Dust (ARD) are studied.

**Keywords:** aerosol scattering, T-matrix, scanning electron microscopy, Mie scattering, particle size measurement

## 1. INTRODUCTION

Laser light scattering is an effective tool for measuring aerosol properties, including the size distribution. Multistatic lidar has been used to measure the size of water droplets in fog and tested for accuracy with aerosolized polystyrene spheres [1-5]. In this paper, we investigate the influence of particle eccentricity and absorption on the ability to measure particle sizes with multistatic lidar. We begin with a microscopy study of Arizona Road Dust (ARD), as it is selected to be a reference material, to identify the range of eccentricity that is expected. Images of dust samples from the Arizona Sonoran Desert are similar in shape, despite being significantly larger in size. Examination of several different samples shows that the results we find are more general. We then perform a model study using T-matrix calculations of optical scattering. The front scattering lobe is found to be almost independent of the particle eccentricity, but does vary with effective size of the particle, for the range of common values found in ARD. This indicates that an approach to measure particle sizes based upon the scattering aureole can be based upon a simple Mie scattering analysis. It will not be sensitive to particle shape, nor is it expected to, since the aureole is dominated by bulk scattering. The advantage is that the eccentricity parameter need not be extracted from the data, so the inversion problem is more tractable. Another situation that we identify as tractable occurs when particles have a size comparable or large relative to the wavelength of the light used. We find that the scattering is independent of particle eccentricity and there is close agreement between T-matrix and Mie calculated results.

One of the most powerful tools used in prior particle size estimation is the polarization ratio of the two scattering phase functions: one polarized in parallel to the scattering plane, and the other perpendicular to it. In experimental studies, it is difficult to accurately measure the absolute light flux. Taking the ratio reduces the problem to making precise measurements. Although it would naively seem that taking the ratio would preclude measurement of the number density, the number density is still measureable. The particle number density influences the polarization ratio through the relative contribution of particle to molecular scattering, since the molecular density and its contribution to scattering is known. Therefore, the polarization ratio data measured over a selected range of angles can be inverted to obtain the number density and other distribution parameters. However, one of the wavelengths used must be short enough that the molecular scattering is not irrelevant. Measurements at several wavelengths can be employed to further increase the confidence of the size/concentration determinations; this is particularly useful when both fine and course size particles are present in a sample. The internal particle resonances that give rise to preferred scattering angles for a given particle size and scattering wavelength are reflected in the phase function and the polarization ratio. This property is what allows accurate determination of size parameters. We find in this study that the resonances are strongly and rapidly depressed by particle eccentricity. Another important case arises when the wavelength of the light used is comparable or large compared to the particle size. No such internal particle resonances exist in this case, so the T-matrix results agree with Mie calculation results and are independent of particle eccentricity when the size parameters much larger than those for Rayleigh scattering. The size parameter is given by $ka$, where $k = 2\pi/\lambda$ for $\lambda$ the wavelength in the medium surrounding the particle with radius $a$. For such particles, a Mie analysis approach is always valid. For particle sizes moderate

Laser Radar Technology and Applications XVIII, edited by Monte D. Turner, Gary W. Kamerman,
Proc. of SPIE Vol. 8731, 87310P · © 2013 SPIE · CCC code: 0277-786X/13/$18 · doi: 10.1117/12.2017710

compared to the range seen in ARD and particles small compared to the wavelength, the angles of maximum scattering intensity do not significantly change as a function of eccentricity, although it should be mentioned that the relative intensity levels at these angles do change with eccentricity. This does not preclude obtaining a measurement inversion, although a T-matrix approach with averaging over a range of eccentricities would likely need to be included. For particles at the upper end of the ARD size distribution, and relatively short wavelengths, the angles of the resonances change as well, and a complicated analysis with many parameters would be required to model the scattering from a particle size distribution.

Another factor besides the scatter induced by irregularly shaped non-spheres that damps the internal particle resonances is absorption, governed by the chemical composition of the particles, which occurs when the imaginary part of the index of refraction is increased. We investigate the scattering properties using T-matrix calculations on spheres. When the imaginary index increases above ~0.01, the resonances are strongly damped. The qualitative behavior is the same as that induced by eccentricity, except the phase function amplitude near the forward direction is reduced as the imaginary index in increased, whereas the magnitude of the forward scattering lobe remains almost independent of the particle eccentricity for values within the range we find in ARD.

## 2. MICROSCOPY OF ARD PARTICLES

### 2.1 Sample preparation

ARD particles (PTI – Power Technology Inc.) were adhered on carbon tape by mounting the tape to the substrate holder, holding it vertically behind a small pile of dust, and then using a puff of air to blow an incomplete layer of particles onto the tape. Areas near the bottom of the tape during deposition and near the top showed little difference in particle parameters, only a lower particle density with height. Some ARD samples were washed in water to remove the smaller particles. ARD ultrafine dust was stirred in a beaker of water, then allowed to settle for a short time (~15 sec.). Since we did not need an accurate size distribution, we did not need to accurately time the process. The Stokes flow rate, $v = 2\Delta\rho g R^2/(9\mu)$, for several micron diameter particles in water is quite fast, so we do not need to use a centrifuge to speed the process. In the equation, $\Delta\rho$ is the difference between the sphere and water density, $g = 9.81$ m/s$^2$, $R$ the particle radius, and $\mu = 0.001$ N s/m$^2$ the dynamic viscosity of water. The smaller particles were decanted with the fluid at the top after the larger particles had been allowed to settle. This process was repeated a few times since some small particles that started near the bottom of the beaker remain with the fallen larger particles. The larger particles were then dried and again resembled a powder, which was applied to the carbon tape in the same manner as the original ultrafine ARD. Sonoran Desert dust samples were obtained as powder and applied without further preparation like that described above for the ultrafine ARD.

### 2.2 Optical microscopy

A Nikon TE-2000U inverted microscope with a 40x, 0.75 NA or 20x, 0.5 NA objective lens and a Photometrics CoolSnap HQ CCD camera were used in reflection mode for the optical microscopy measurements. Figure 1(a) is a typical example of what is observed for ARD. There is a large number of free and clustered small particles, and hints of larger particles hidden beneath. The resolution is not good enough to make an accurate judgment of the eccentricity or aspheric nature of the particles, but enough to qualitatively conclude that the mid-larger sized particles are not too far from spheres. The SEM data, which has higher resolution, is more precise about this. In order to better observe the mid-large sized particles, we need to remove the small particles. We do this by washing. The larger particles settle out quickly in water, and can be viewed when separated and dried. An image of the larger particles is given in Figure 1(b). It is now easier to discern the near-spherical mid-sized particle shapes and the larger particles. Since the optical microscope has a short depth of focus – shorter than the height of the larger particles, the larger particles are not fully in focus. This gives them the appearance of being taller than they are wide. The focusing mechanism on the microscope is calibrated, so the height can be accurately measured by focusing on the particle bottom (and tape surface), then measuring the change in height required to focus at the top of the particles. When this is done, most particles are found to have an eccentricity in the range 1.0 – 1.5, similar to that viewed in any image plane as the ratio of the lateral distances.

The apparent stretching of the height is much more apparent in Sonoran Desert dust, which contains larger particles than Ultrafine ARD. A sequence of images is shown in Figure 2, during which the focus is changed from a focus at the level of the tape in Figure 2(a) to 60 microns above it in Figure 2(d). A further focus adjustment of 30 microns is required before the tops of the tallest (and widest) particles are in focus.

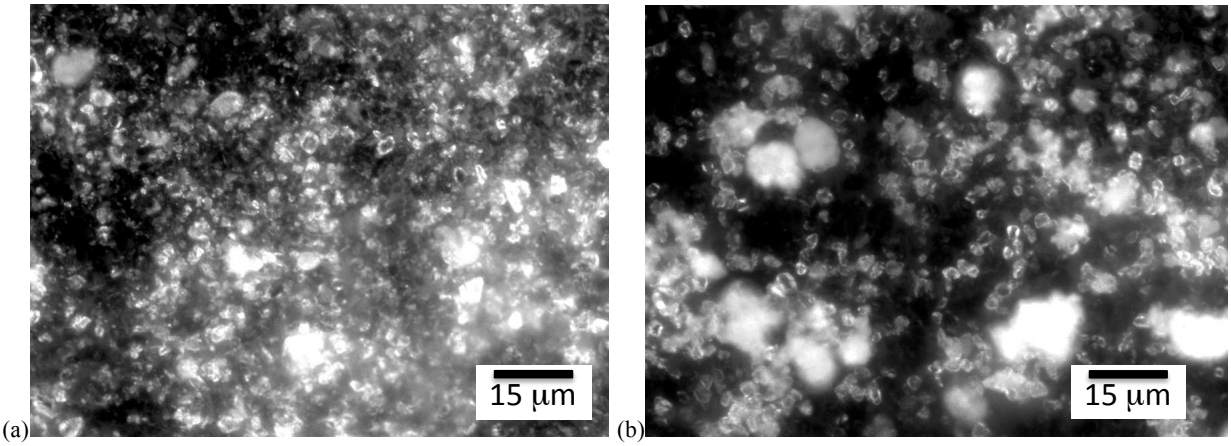


Figure 1. Optical micrographs of ARD; (a) ultrafine ARD at 40x shows a significant number of smaller particulates and a few larger ones, (b) after washing to remove some of the smaller particles, the larger particles are visible. Note the eccentricities are close to 1.0, with a few outliers larger than 1.5.

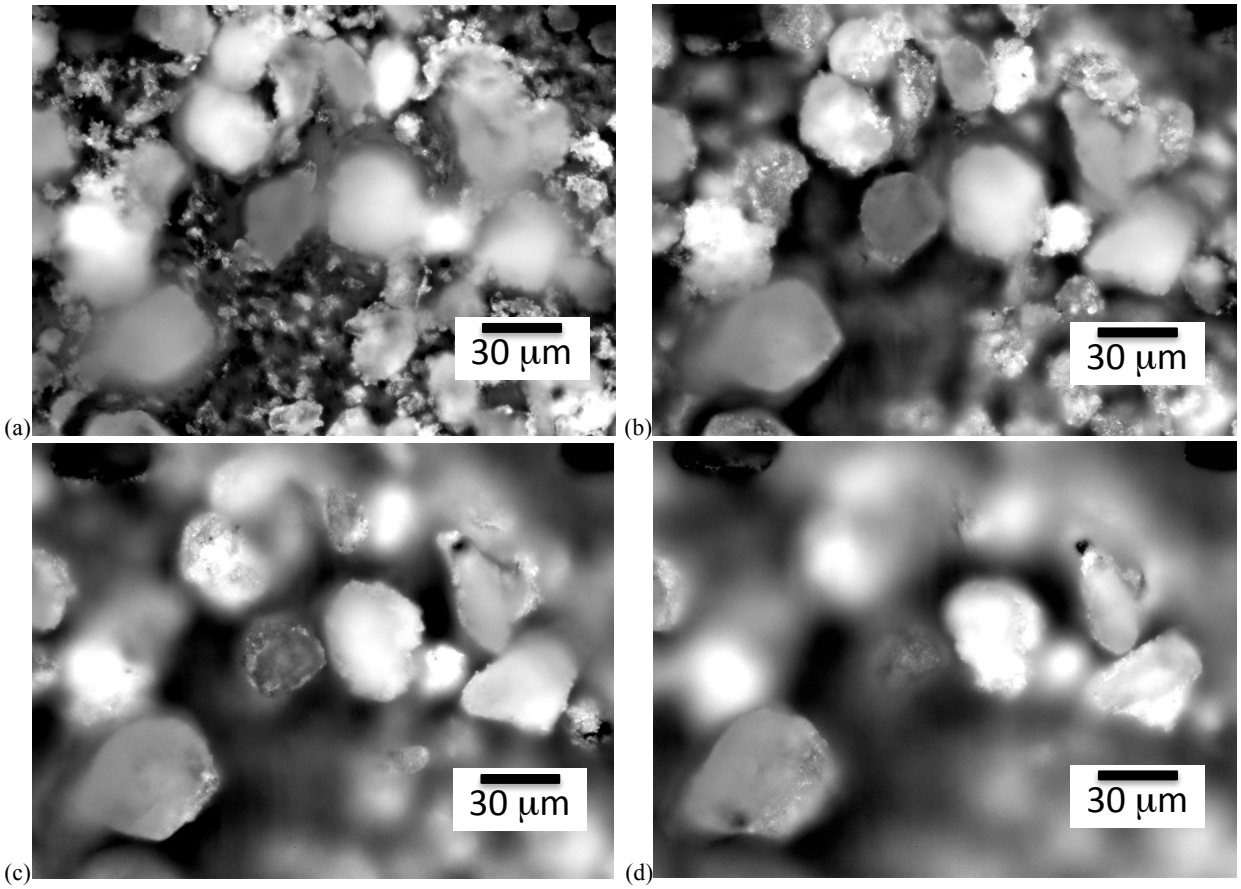


Figure 2. A sequence of optical micrographs of Sonoran Desert dust is taken at the same location but with a focus adjustment so that the vertical extent of the particles can be measured. The short focal depth of the microscope (20x, 0.5 NA objective) causes the particles to appear taller than they really are: (a) At 0-microns, the tape is visible between the larger particles, as are very small particles stuck to it. (b) At 20 microns, the tops of some of the smaller particles are visible, but the larger ones show a cross-section. (c) At 40 microns, the smaller particles are out of focus, the largest still cut off. (d) At 60 microns, a few more particle tops are in focus, whereas others will need another 30 microns of focus change to find the tops. Note here also, the eccentricity evident in the cross sections and vertical size measured by focus change are again close to one for most particles, although these particles are much larger than the ARD particles.

Our aim with these images is to obtain a range of the eccentricities of the particles. The lateral dimension is most easily observed in the cross-sections of the particles when the focus is near the center of the particle along the focus direction. Several images, at different focus distances, are required, as in this figure, since the particles have different heights. Size in the vertical is compared by focus adjustment. The results are consistent with those above – the departure from spheres is typically less than a factor of 1.5, with a few up to ~2. This is typical of all areas observed. The departures we have seen usually involve the extremities of particles, where sharp corners are sometimes observed, or a particle might flatten towards one end. In three dimensions, these are similar features. The general particle shape beneath is still closer to a sphere, however, so these asperities will be similar to the decoration of the larger particles by smaller ones, which is a feature regularly observed on the unwashed samples, and sometimes observed on the samples washed in water.

### 2.3 Scanning electron microscopy.

Scanning electron microscopy provides a higher resolution than optical microscopy, so the decoration of the larger particles by smaller ones can be studied in more detail, as can the shapes of the smaller particles. Whereas the particle height apparently stretches due to the short focal distance of the optical microscope, the SEM flattens the particles in the images due to its long focal length compared to the particle height. Figure 3(a) shows a large area view of a sample of ultrafine ARD. It is typical, and gives a good indication of the range of particle shapes that are found. A few of the particles have eccentricities close to 2, but most are smaller. Sharp corners are again a more prevalent departure from a spherical form, as was observed in the optical micrographs. Although the ultrafine particle size distribution is supposed to include sizes up to 15 microns, we observe very few close to that. The number distribution peak of Ultrafine ARD, according to its documentation, is ~2-4 microns, and agrees qualitatively with what we observe here. A higher resolution image at a different location is shown in Figure 3(b). Besides the same general features noted in conjunction with Figure 3(a), the decoration of the larger particles by smaller ones is easily observed. The smaller particles adhered to the tape between the larger particles are also more easily observed.

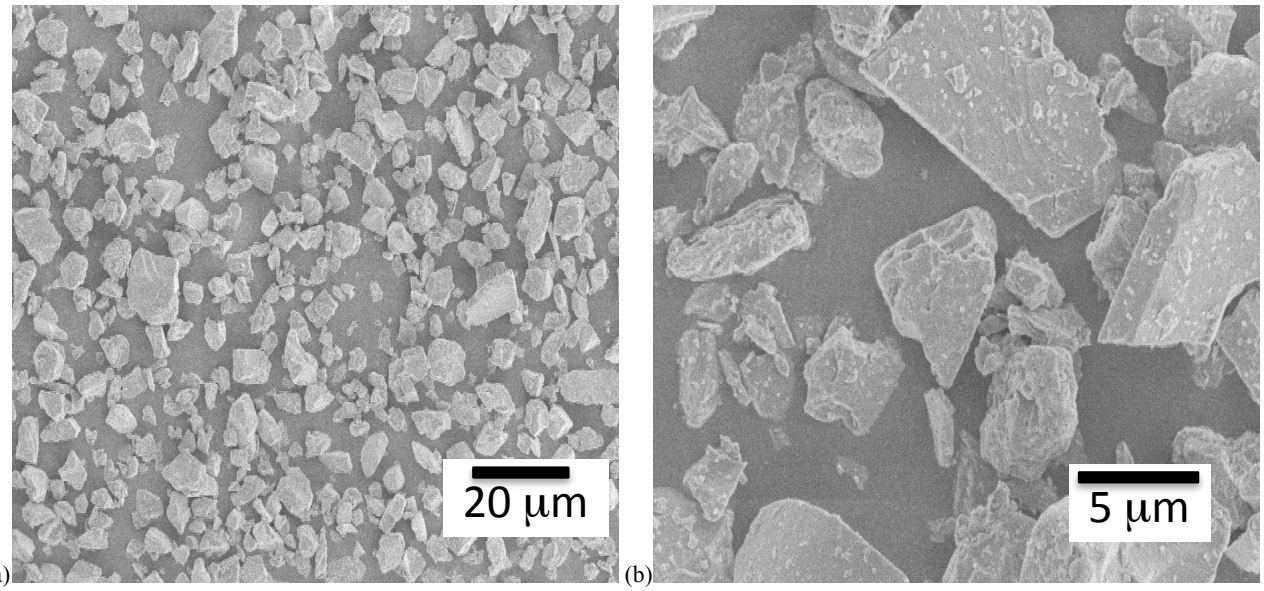


Figure 3. Scanning electron micrographs of ultrafine ARD appear flattened by the long focal length of the SEM. The eccentricity of the particles is consistent with the optical microscopy, with most less than 1.5 and a few outliers near 2. Sharper features are also observed with the additional resolution of the SEM. Again, the larger particles are decorated by smaller ones: (a) A large area view gives statistics on the particle shapes. (b) A zoom-in illustrates the decoration and smaller particles between larger ones. Although some particles appear 'layered,' this is a long focal length 'flattening' artifact, as can be seen on the tilted particle at the center right, the 'ledges' are really foreshortened decorating particles.

A quick look at several of the particles such as those in the cluster just to the right of center in Figure 3(b) would suggest a layered nature for the particles. This is where it is important to understand the flattening effect in SEM imaging. The apparent layers are actually the edges of smaller, decorating particles that are foreshortened in the vertical direction until they appear to lie along a line. This can be proven in several ways. A higher magnification is shown in Figure 4, where the shorter focal length results in less flattening. When viewed at higher magnification levels, some will be slightly out

of focus and thus appear to separate. Although easily observed when adjusting the focus back and forth, this is hard to capture in fixed images, another method is to look for tilted particles. Several such regions are observed in this image, note the two larger particles near the top and near the bottom of the right side of the image. No layering is observed, but both sides have attached smaller particles. Note that no measurement of the relative lengths of the sides can be made using the tilted particles unless the tilt angle is known. The perspective is apparently due to the relative location of the electron detector relative to the sample normal (so that the different faces have different brightness). Due to the flattening of the image, it is easy to measure projected lengths rather than true sizes.

To make quantitative size measurements and to verify that the tilted particles are not different from those resting more precisely on one face, the sample must be tilted. Images are taken at different tilt angles, and the precise orientation and dimensions of a particle can be obtained. Using an SEM in this mode is tedious and time consuming, but we show an example in Figure 4. A top-down image near normal incidence to the tape surface is shown in Figure 4(a). From this perspective, it is not clear if there is one large particle with a complicated shape, or if there are several particles. In particular, the lower left side seems to show an attachment. After sample tilting of the normal out of the page to the right by 35 degrees, a second image is taken, Figure 4(b). Several observations emphasize the above points: The particles are not attached. The left face of the largest of the three particles is much larger in the horizontal dimension than it looked before. It is also much flatter, and decorated with surface-adhered smaller particles. It does not look layered as it did, but rather resembles more the right face, which in the tilted image has itself taken on more of a layered appearance. Similar conclusions result from a careful examination of the other particles in the figure, which have also been tilted. Along most of the bottom of the image is a defect in the tape. This appears layered in both tilts, and thus probably really is layered. Layers are expected for defects in tape. These defects appear throughout the tape, even above where particles are blown, and tend to catch particles more effectively than the flatter areas of tape. Note the relatively larger number of small particles in the defect.

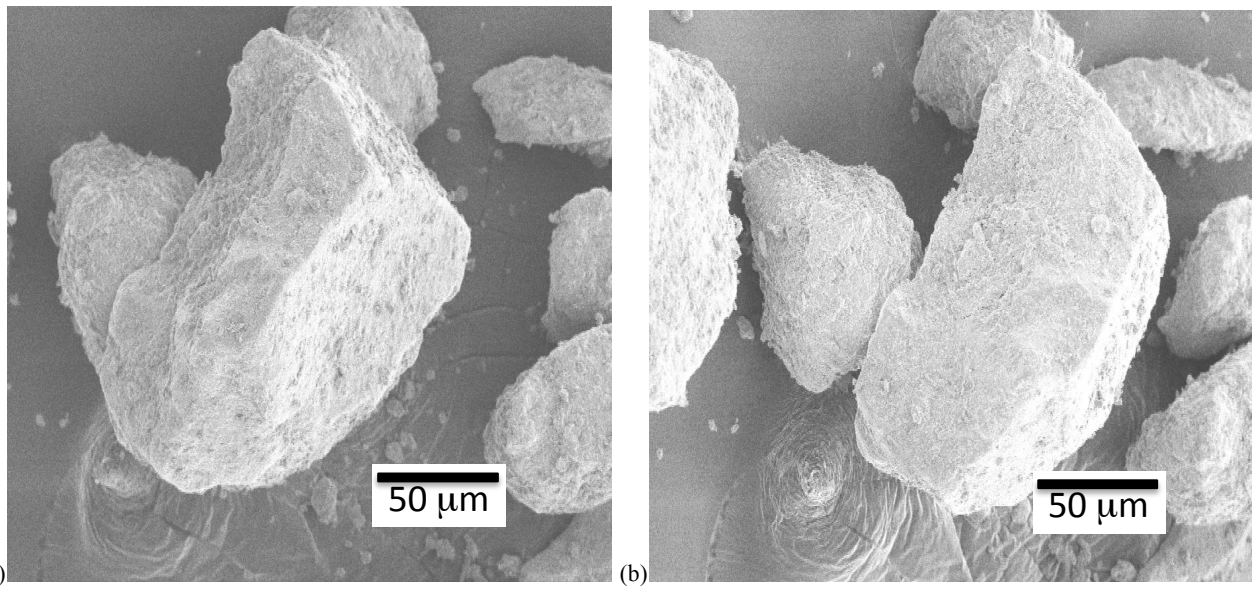


Figure 4. Two SEM micrographs of the same particles: (a) The top-down view shows the edge and two sides. (b) Once the sample is tilted 35 degrees so that the face on the left is seen more head-on, the apparent layers are observed to be really foreshortened smaller particles on the face. It is also seen that the two particles beneath the larger are actually separate from it.

## 3. NUMERICAL STUDY OF THE EFFECTS OF ECCENTRICITY

In the previous section, we found that the particles of several dusts over a large size range do not have large eccentricities, <2.0, but the typical eccentricities are less than 1.3-1.5. In this section, we study the effects of eccentricities in this range on the scattering phase functions and the polarization ratio of these phase functions. To the

extent that they are not impacted, the simpler (and with fewer-parameters) Mie formalism can by used to perform an inversion to obtain particle size distribution information. We use the T-matrix method for computations here.

### 3.1 T-matrix method

We used the publically available T-matrix code of Mishchenko [6] that has been modified. The first modification, proposed by Moroz [7], involves a different routine to perform matrix inversion. It has been found to greatly improve the convergence when the particles are highly absorbing. Although it is not critical for this work, it will be useful for ARD modeled over larger wavelength ranges, since silica exhibits strong absorptions at LWIR wavelengths. Convergence near those wavelengths will be adversely affected near those wavelengths for pure silica. In the normal case of mixed composition, an effective medium approximation can be used – as long as the variations in composition are on size scales of ~$\lambda$/10 or less. The effective index will typically have much less dramatic variations, and often a shift in the sharp absorption features will result. We put the Moroz modifications into the newer (LAPACK) Mishchenko code that calculates the distributions [8] (not the single orientation modification of the older Mishchenko code available online).

The second modification includes the calculation of the polarized components of the scattering phase functions and their ratio in the program, and a conversion to a command-line and to an input file driven program that does not need to be recompiled for each data set. The resulting program can be called from another program to make batch calculations and data manipulation more automated.

### 3.2 Polarization ratios

The polarization ratio of the scattering phase functions removes many experimental factors that are difficult to quantify. We study the effect of particle eccentricity on the polarization ratio. The polarization ratio is the scattering phase function for incident light polarization parallel to the scattering plane (the plane that contains the incident light ray and the line between the scatterer and the detector) divided by the intensity of the scattering phase function for polarization perpendicular to the scattering plane. This choice is made since the perpendicular phase function is a constant for Rayleigh scattering while the parallel one follows a cosine form – in particular, it is zero at 90 degrees. Thus, the ratio remains finite for Rayleigh scatterers. The use of a single particle size engenders large features in the polarization ratio where the perpendicular phase function nears zero, as we observe here. They are not nearly as significant when a distribution of sizes is used, since the perpendicular phase function has zeroes at different angles for different sizes. We examine a single size particle for clearer insights into the behavior as a function of the particle size parameter, but the measurements include scattering from an ensemble of particle sizes, which reduces the magnitude of the oscillations.

Our simulations use a fixed particle size of 2-micron area-equivalent spherical particle diameter. The reason for choosing an area-equivalent diameter is to keep the overall scattering cross section reasonably constant (although variations in scattering efficiency occur). Four wavelengths are simulated: 0.532 microns, which has a size parameter ka~12, and is somewhat smaller than the particle size; 1.064 microns or ka~6, about the radius of the particle, 4-microns or ka ~ 1.5, and 10 microns or ka ~ 0.6, small but not yet in the Rayleigh regime. The eccentricity values examined are between 1.0 (spheres) and 2.0 (approximately the largest value observed in SEM images), with more values chosen closer to 1.0, consistent with more particles having those values. An index of refraction of 1.5 + 0.0001i is selected for the particles.

The peaks of the calculated polarization ratio values, shown in Figure 5(a), are very large for spheres at 0.532 microns. If a distribution of sphere sizes was used, this would not be the case, as the peak positions in the scattering phase function would wash out the near zero points in the perpendicular-polarization phase function. As particle asymmetry increases, the maximum abruptly drops, by a factor very close to 60 as the eccentricity increases from 1.0 to 1.05. The decrease beyond that is still rapid, and is shown in Figure 6. It is interesting to note that the peak with the largest maximum is actually at a different angle for an eccentricity at 1.05 compared to 1, 1.1 and 1.3. This is observed in Figures 5(a) and 6. The form of the polarization ratio does not change dramatically for any of the eccentricity studied, although it is somewhat different for 1.3 and 2.0 compared to the more spherical particles.

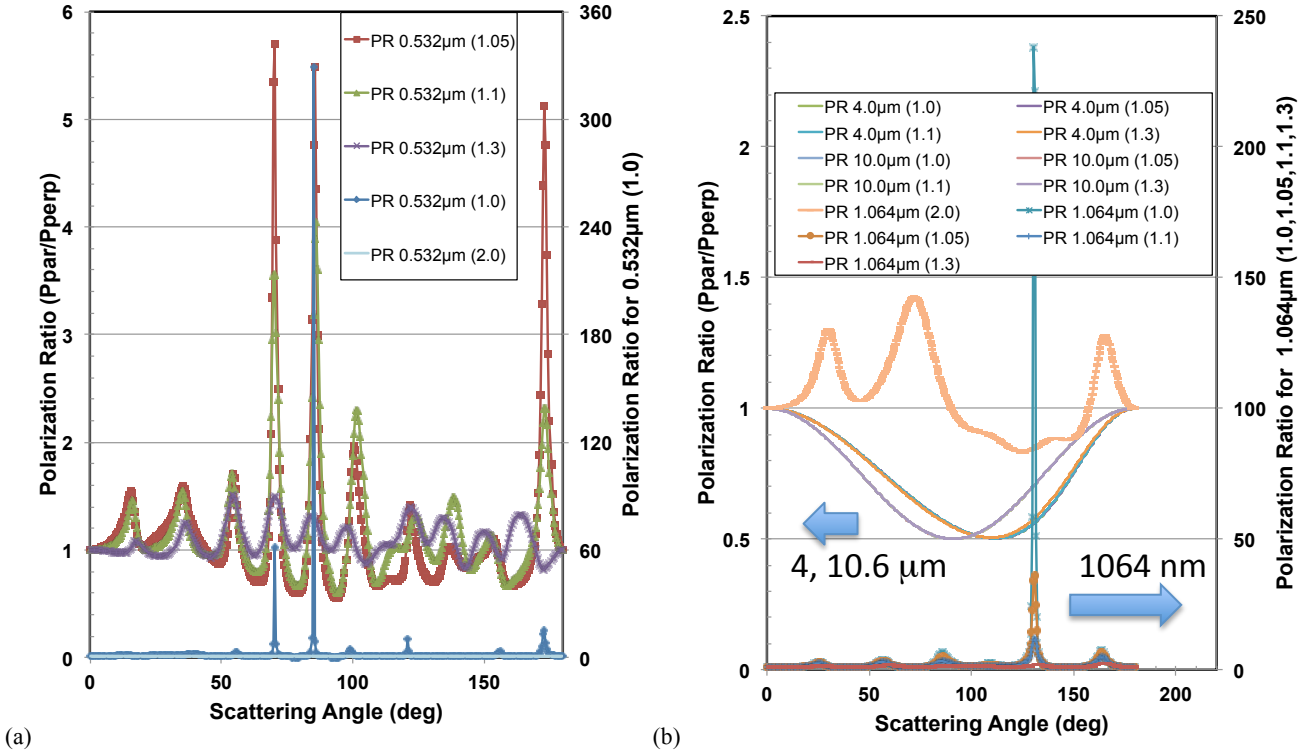


Figure 5. Calculations of polarization ratios (PR) of scattering phase functions at 0.532, 1.064, 4, and 10.6 μm are shown for a volume equivalent 2-μm diameter sphere. The wavelengths and eccentricities (in parentheses) are given in the legend: (a) At a visible wavelength of 0.532 microns, the phase function amplitude decreases so strongly with eccentricity that the spherical case is plotted on the right axes while the others are plotted on the left axis with 60x less range. (b) The variation with eccentricity is less in the infrared. The results for all but the most eccentric ellipsoid at 1.064 microns are plotted against the right axis, while the 1.064 micron polarization ratio is plotted on the left axis to illustrate the shift in peak position. The data at 4-microns all lie on top of each other, as do those (separately) at 10 microns.

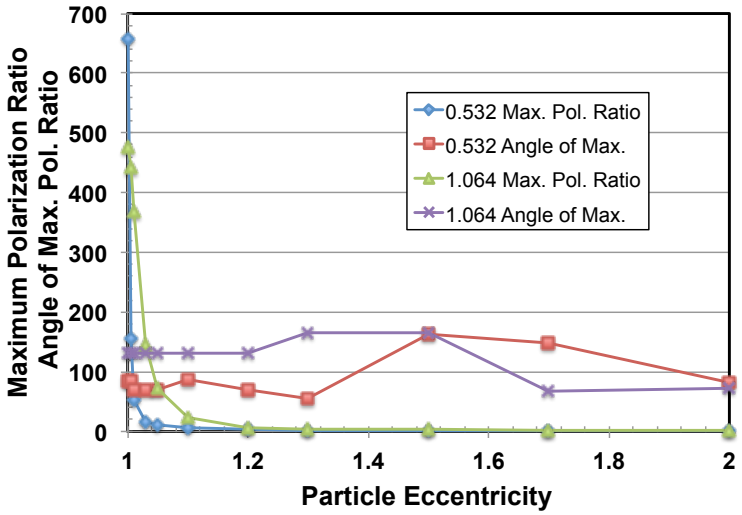


Figure 6. The maximum in the polarization ratio is shown as both a value and as the angle at which it occurs versus the eccentricity of the particle. A few steps in the angle at which it occurs results from a different variation of the various maxima with eccentricity, so a different maxima becomes the overall maximum. The magnitude is observed to strongly decrease at visible and, more slowly, at near infrared wavelengths. The sphere area-equivalent particle diameter is 2 microns.

The results for 1.064 microns, shown in Figure 5(b), are similar to those for 0.532 microns, only less dramatic. The other notable point is that there is a large qualitative change in the form at the largest eccentricity of 2.0 compared to the others. The data for 4-microns all lie on top of each other. The form of the polarization ratio is far from the cosine function of Rayleigh scattering. The minimum in the ratio is not even at 90 degrees, and is far from zero. At 10 microns, a more Rayleigh-like form with the minimum at 90 degrees is present, but the value there is still far from zero.

In summary, the polarization ratio shows a dramatic change even for very small amounts of eccentricity in particle shape for wavelengths smaller than the particle size, but as the particle size parameter approaches 1.0, the polarization ratio becomes independent of the size parameter. In this regime, therefore, Mie scattering calculations can be used to obtain essentially exact results.

### 3.3 Scattering phase function

The polarization ratio results lead us to expect that the particle resonances at angles that depend upon the size parameter will quickly diminish with particle eccentricity. We find that they do diminish, but much more slowly. Further, we find that the reason for the polarization ratio becoming independent of eccentricity is that there are no more resonances at those size parameters, so the scattering phase functions also become independent of the eccentricity. For larger size parameters, the forward scattering lobe, and to a lesser extent the first side lobe, are only weakly dependent on the eccentricity. The width of the forward lobe does depend upon the size parameter; however, which means an estimate of particle size is embedded in a measurement of this quantity, i.e. the scattering aureole. The simulation parameters are the same as above.

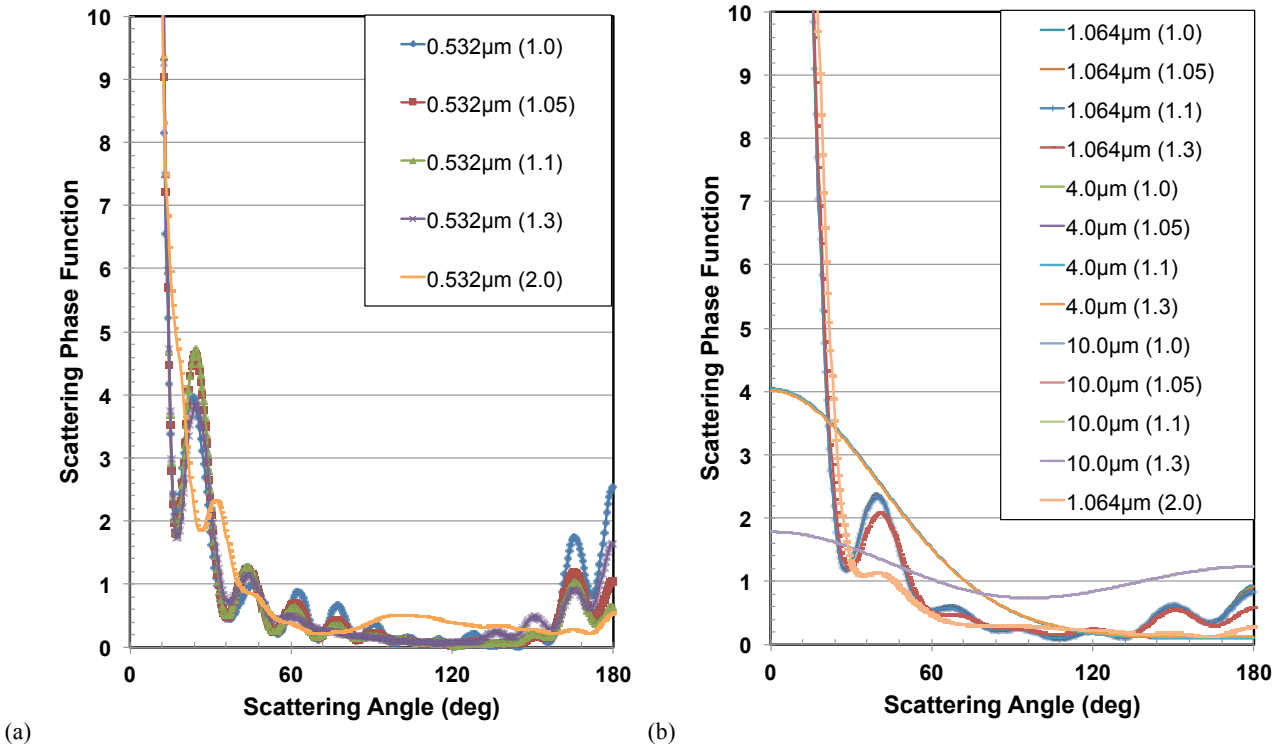


Figure 7. Scattering phase functions versus angle. The wavelengths and eccentricities (in parentheses) are given in the legend: (a) The resonances decrease slowly with eccentricity after an initial drop, for a size parameter near 12, but remain qualitatively the same until the eccentricity reaches ~2, which was rarely observed in ARD Ultrafile samples. (b) The dependence is increasingly weak for longer wavelengths, or smaller size parameters (~ few to less than one), until there is none at all. Notice the lack of dependence on eccentricity begins long before the particles enter the Rayleigh regime. This occurs even before symmetry in the front and back scattering is approached, and well before a value of zero is reached at 90 degrees.

Figure 7 shows the results for the scattering phase function calculated for the selected values of eccentricity. The shorter wavelength, larger size parameter, results in part (a) do show a significant decrease in the amplitude of the magnitude of

the resonance peaks versus angle, when compared to particles with even a small eccentricity. However, they do not go to zero, but saturate at a new level until the new resonances in the perpendicular directions become significantly different, and the resonance locations shift to other angles. Since we are using particles with constant area-equivalent spheres, the sizes change, and so do the resonance locations as expected. The onset is more abrupt than naively may be expected. The longer wavelength, smaller size parameter, results are shown in part (b). The dependence is again weaker than those at a larger size parameter, and it is in fact largely independent of particle eccentricity. This is not surprising for size parameters close to 1.0, where the scattering lacks peaks due to particle resonances. The data for 1.064 microns is rather striking, with significant deviations only for eccentricities above ~1.5. Not shown in the figure is the height of the forward lobe, which for the x ~ 12 sphere case is marginally above the non-spheres, which are all virtually identical. At the smaller size parameters studied, the forward lobe peak is independent of eccentricity and agrees with the spherical result.

In summary, the forward lobe is almost independent of particle eccentricity for all eccentricity and size parameters studied. For large size parameters, there is a significant change at all other angles, including backscatter. For smaller size parameters, ka~ 6, the scattering phase function is almost independent of eccentricity until the eccentricity is on the tail of the observed eccentricities for ARD. This implies applicability of Mie based analysis for these data.

## 4. NUMERICAL STUDIES OF THE EFFECTS OF IMAGINARY INDEX

The presence of an imaginary index will damp light as it propagates in particle resonances, and hence may be expected to cause similar behavior as non-spherical particle shape – which can also be thought of as scattering energy away from the spherical resonances. We therefore perform a computational study of its effects. We use the same particle sizes and wavelengths as those used above, but use spheres only, and vary the imaginary component of the complex index of refraction from the 0.0001 used above to 1.0. We find that the dependences are weaker and qualitatively different.

### 4.1 Polarization ratio

The maximum value of the polarization ratio, shown in Figure 8, is plotted against a logarithmic axis for the imaginary index since absorption is an exponential process. The magnitude decreases with increasing index, although not monotonically. There is an odd point at 0.05*i* that is not present at 0.04*i* or 0.06*i*, and is associated with a narrow, low but nonzero (12 degrees) angle mode. The polarization ratios themselves do not show much qualitative change except enhancement of that 12 degree mode until 0.07*i* and above, where the peaks below ~60 degrees become dips, and above ~1.0*i*, when shifts in resonance positions are observed and amplitudes are greatly diminished.

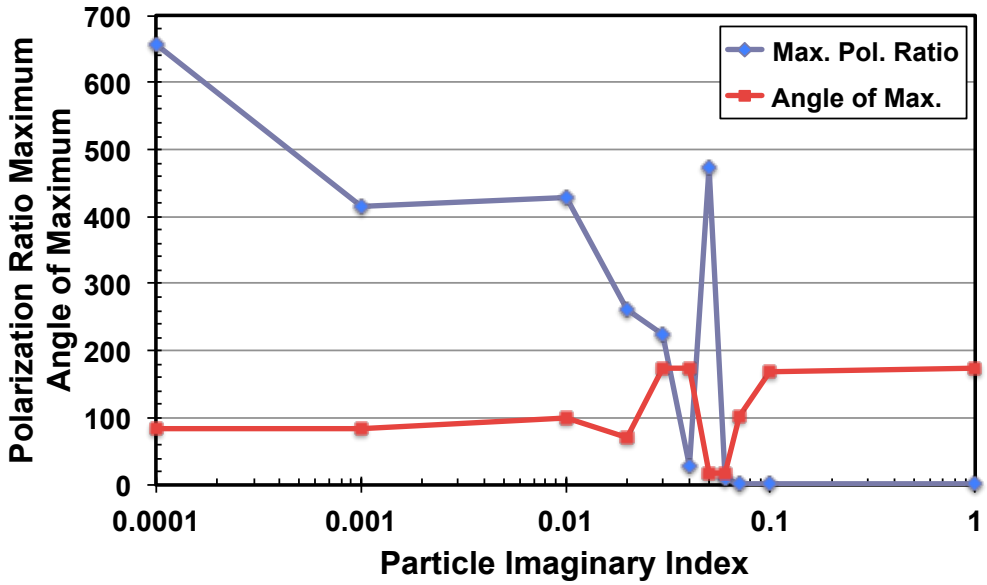


Figure 8. The maximum value of the polarization ratio and the angle at which it is attained are shown as a function of the imaginary index. Note the log scale on the horizontal axis.

### 4.2 Scattering phase functions

The scattering phase function calculations are shown in Figure 9. Contrary to the eccentricity results, we find the height of the forward lobe is strongly impacted by the imaginary index. Similar to the eccentricity results, the width of the front lobe is not dependent upon the parameter varied. Little difference is observed for imaginary index below $0.1i$ at any angle except for some damping. At $0.1i$ and above, the damping is stronger and shifts in resonance angles are observed. The primary feature of note, besides the magnitude dependence of the forward lobe on imaginary index, is the even stronger dependence on it in the backward lobe, which is almost completely damped above ~$0.01i$.

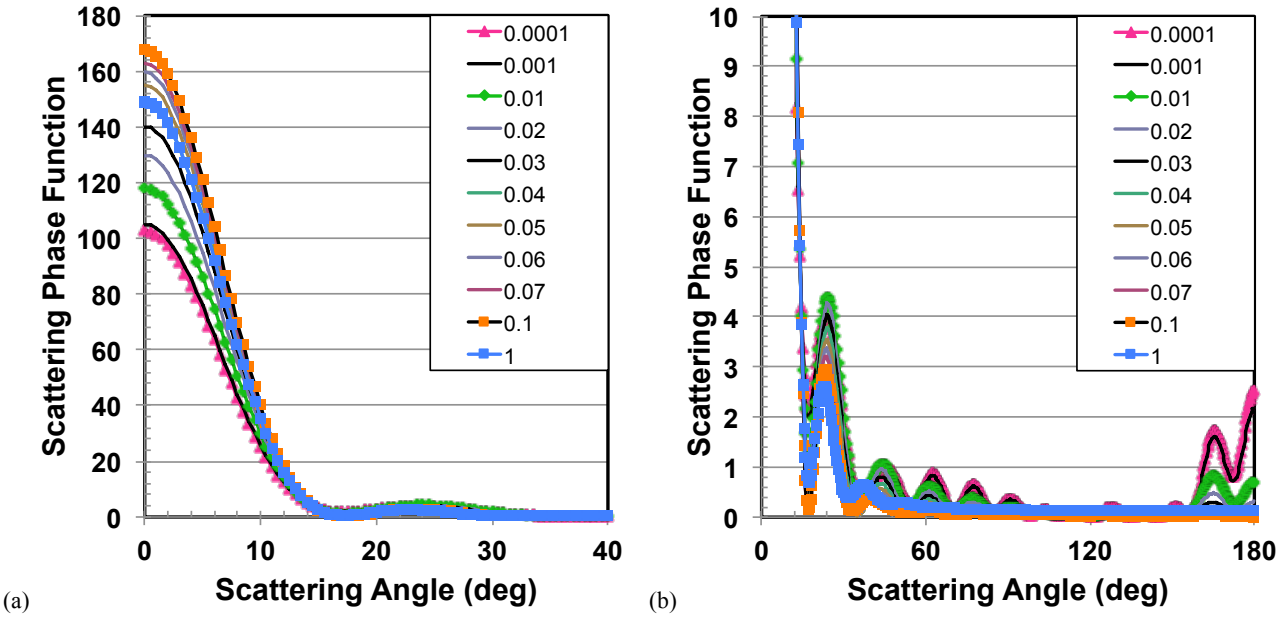


Figure 9. Scattering phase function versus angle is plotted for several imaginary index values noted in the legend. Little differences are observed for imaginary index below $0.1i$, except for some damping. The damping is stronger and shifts in resonance angles are observed for $n_k > 0.1i$: (a) The graph is scaled for observation of the aureole. (b) Another scaling emphasizes the backscatter and changes at large damping.

## 5. EXPERIMENTAL DATA ON NONSPHERICAL PARTICLES

The scattering from ARD particles lofted into the air in a test chamber is measured. Both the near-forward scattering aureole and the scattering near backscatter are measured to illustrate the properties identified in the modeling computations above. Such experimental measurements by necessity involve a distribution of particle sizes and a range of eccentricities. However, the qualitative trends will be evident.

### 5.1 Experimental set-up

A cylindrical chamber is equipped with fans to swirl the air and provide vertical mixing to create a quasi-uniform dispersal of aerosols for study. The chamber has an entrance and exit windows for both laser beam entry and exit and camera viewing of the beams in the scattering volume. Canon EOS cameras capture the scattered light at a known relative location and angle with respect to the laser beams and the scattering volume. The raw images are analyzed to obtain the extinction-corrected scattered light from each volume within the uniform dust aerosol intercepted by the laser beam. The corrections yields a quantity comparable to, up to a scaling factor, the average of the number times cross section times the polarization phase function. Mie calculations for comparison are also averaged over the corresponding APS-measured size distribution to obtain the equivalent quantity. The Mie calculation assumes that the particles are spheres, have an index of refraction equal to that of silica, and have the size distribution measured by the APS unit. These volumes are labeled by their scattering angle and presented below. Several screened size cuts of ARD are tested. Different masses of dust are used to create different dust density scenarios for each of these size cuts. The dust settles in

the chamber over time. Size distributions were measured with an aerosol particle sizer (APS) unit, and examples are shown in Figure 10.

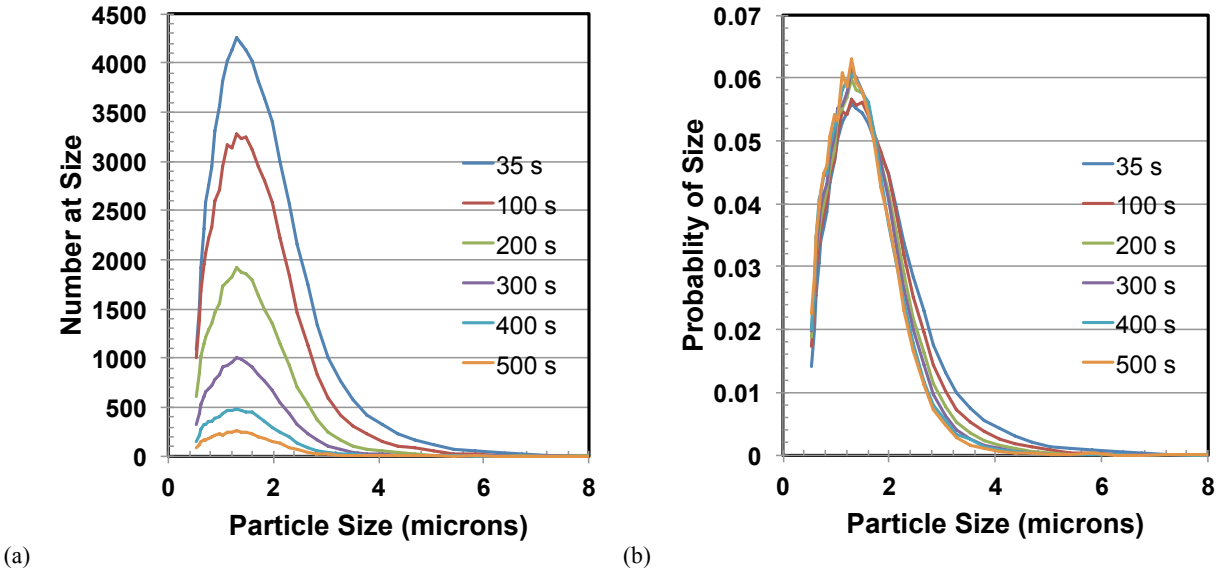


(a) (b)

Figure 10. The particle size distribution is shown at several times after injection of 0-5 micron sieved ARD. This serves to give an indication of the settling time of the dust for understanding the meaning of the time values below. (a) The raw counts, (b) the same data normalized to unity integral, so represent a probability distribution and make clear the relative reduction of larger particles in time.

### 5.2 Scattering phase functions

Typical scattering phase functions for 532 nm incident light and the 0-5 micron sieved ARD is shown in Figure 11. The times after aerosol injection and size distributions present correspond to those in Figure 10. As expected from the above computations, the non-spherical nature of the particles results in a decrease of the oscillation magnitude of the phase function compared to the spherical assumption. As time passes, two properties of the particle size distribution change. The first is an overall decrease due to settling. The second is a trend towards smaller particles on average, since the large particles will drop out more quickly according to the same Stokes law reasoning presented earlier (but here in air). Smaller particle are expected to have a broader aureole. That is what is evident in the measured data.

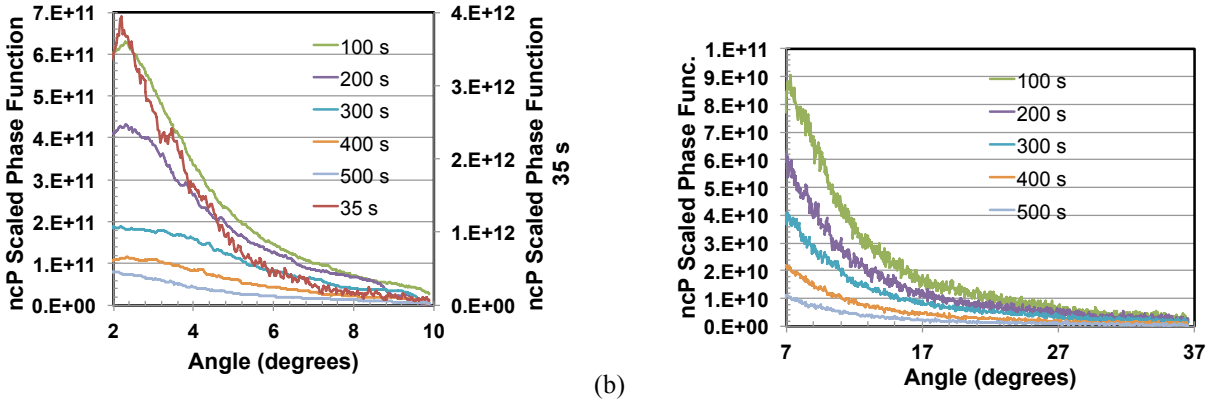


(a) (b)

Figure 11. Scaled scattering phase functions, corresponding to the number density times the cross section (both averaged) times the phase function, versus angle is plotted for (a) s-polarization, the data for 35 s is plotted on the right axis to better show the changes of the width of the forward lobe, and (b) p-polarization, with a larger angle range.

### 5.3 Aureole

The aureole is expected to retain agreement with the spherical assumption of the Mie calculation, according to the above computational analysis. Figure 12 shows a plot of the measured aureole at 500 seconds and a Mie calculation that uses the size distribution given above. It has only one free parameter, a scaling due to the detector sensitivity. The agreement is quite good. The discrepancy between the calculation and the measured data is likely due to a wrong index of refraction for ARD used in the calculation. Since a value could not be found in the literature, we simply used the value for silica, a major component. Use of a higher index would steepen the curve and provide better agreement.

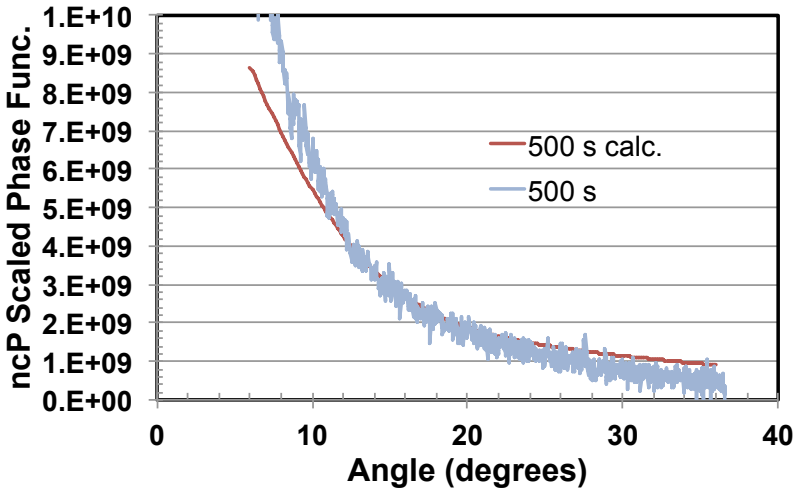


Figure 12. Scaled scattering phase function versus angle at small angles, the scattering aureole, is measured and plotted along with the a Mie calculation based upon the measured particle size distribution and using silica's index of refraction for the ARD.

### 5.4 Large Angle Scattering

The computational results above suggest that the scattering at large angles should not be well modeled by Mie calculations when the particle sizes are not smaller than the wavelength. The measurements and Mie calculation are shown in Figure 13, and the two agree better than expected since 532 nm is several times less than the mean particle size. In particular, the general trend of the two polarization data sets is different, but captured in the calculated scattering.

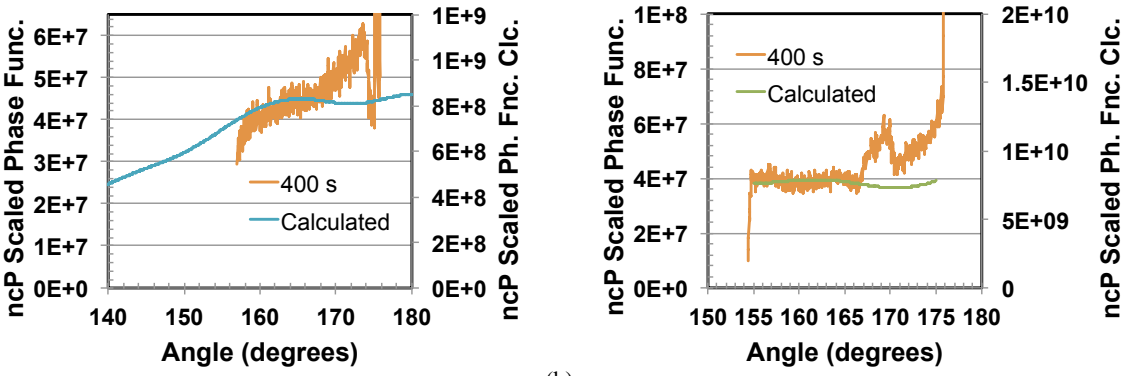


Figure 13. The near-backscatter, measured, scaled (as in Figure 11) polarization ratio of 0-5 micron sieved ARD, known to have a range of eccentricities, is compared to the spherical assumption given by the Mie calculation. As expected from the computations above, the agreement is not very good. The model uses the index of refraction of silica and the APS size distribution at that time, shown in Figure 10. (a) The s-polarization has a background slope as does the Mie calculation. (b) The p-polarization has a flat background as does the Mie calculation. There is an arbitrary scaling of the calculation.

## CONCLUSIONS

An experimental study with both optical and electron microscopy has revealed the range of particle eccentricities to be small (eccentricity <2.0 and mostly less than 1.1) for ARD and Sonoran Desert dusts. We use these limits to choose bounds for a computational study on the effects of particle asymmetry on the polarization ratio and scattering phase functions. These two useful quantities that can be inverted to obtain information about the particle size distribution and particle concentration when the background air Rayleigh scatter is also measured. We find that a spherical analysis, based upon Mie scattering calculations, is valid when the particle size parameters are close to or smaller than 1.0. For larger size parameter, the forward lobe is still almost independent of the eccentricity, indicating that scattering aureole measurements may also be analyzed by a Mie scattering based inversion. The introduction of significant imaginary index of refraction does not change the aureole width, but does damp the forward scattering intensity. Backscatter is also found to be strongly damped. Measurements of scattering from ARD display features similar to those modeled.

## REFERENCES


[1] Brown, A. M., Snyder, M. G., Brouwer, L., Philbrick, C. R., "Atmospheric aerosol characterization using multiwavelength multistatic light scattering," *Proc. SPIE* 7684, Laser Radar Technology and Applications XV, 76840I, doi:10.1117/12.850080 (2010).

[2] Philbrick, C. R., Hallen, H., Wyant, A., Wright, T., Snyder, M., "Optical remote sensing techniques characterize the properties of atmospheric aerosols," *Proc. SPIE* 7684, Laser Radar Technology and Applications XV, 76840J, doi:10.1117/12.850453 (2010).

[3] Philbrick, C. R., Wright, T., Snyder, M., Hallen, H., Brown, A. M., Verghese, S., Edwards, P. S., "Characteristics of atmospheric aerosols using optical remote sensing," 90th American Meteorological Society Annual Meeting, (2010). https://ams.confex.com/ams/90annual/webprogram/Paper163441.html

[4] Snyder, M. G., Brown, A. M., Philbrick, C. R., "Sensitivity of the polarization ratio method to aerosol concentration," *Proc. SPIE* 8037, Laser Radar Technology and Applications XVI, 80370K, doi:10.1117/12.884206 (2011).

[5] Philbrick, C. R., Hallen, H., Snyder, M., Brown, A. M., "Remote sensing of atmospheric aerosol properties," 91st American Meteorological Society Annual Meeting, Third Symposium on Aerosol-Cloud-Climate Interactions, (2011). https://ams.confex.com/ams/91Annual/webprogram/Paper186827.html

[6] Mishchenko, M. I. and Travis, L.D., "Capabilities and limitations of a current FORTRAN implementation of the T-matrix method for randomly oriented, rotationally symmetric scatterers," J. Quant. Spectrosc. Radiat. Transfer 60(3), 309-324 (1998).

[7] Moroz, A., "Improvement of Mishchenko's T-matrix code for absorbing particles," Applied Optics 44(17), 3604-9 (2005).

[8] Mishchenko, M. I., Travis, L.D., and Mackowski, D. W., "Electromagnetic Scattering by Particles and Surfaces: T-Matrix Codes for Computing Electromagnetic Scattering by Nonspherical and Aggregated Particles," NASA Goddard Institute for Space Studies, http://www.giss.nasa.gov/staff/mmishchenko/t_matrix.html